Journal of Computing and Electronic Information Management
ISSN: 2413-1660 | Vol. 16, No. 3, 2025

Simulation analysis of the effects of aerosol and surface albedo on the remote sensing detection of greenhouse gases in the short-wave infrared 1.6 μm

Min Li[1, 2], Leiku Yang [1 *], Zhengqiang Li [2], Cheng Fan [2], Zihan Zhang [2], Qingyun Liu [2], Yundong Xuan[3], Jiantao Dong [4] and Zheng Shi [5]

[1] College of Surveying and Land Information Engineering, Henan Polytechnic University, Jiaozuo 454003, China
[2] Key Laboratory of Remote Sensing and Digital Earth & Key Laboratory of Satellite Remote Sensing of Ministry of Ecology and Environment, Aerospace Information Research Institute, Chinese Academy of Sciences, Beijing 100101, China
[3] School of Emergency Management Science and Engineering, University of Chinese Academy of Sciences, Beijing 100049, China
[4] Satellite Application Center for Ecology and Environment, Ministry of Ecology and Environment of People's Republic of China, Beijing 100094, China
[5] The Administrative Center for China's Agenda 21, Beijing 100098, China

[*] **Corresponding author**: Leiku Yang (Email: yanglk@hpu.edu.cn)

Abstract: Aerosols and surface albedo are major sources of error in retrieving greenhouse gas concentrations using high-resolution shortwave infrared spectroscopy. This study employs a high-precision atmospheric radiative transfer model to simulate the influence of aerosols and six different surface types on satellite-observed spectra in the 1594 nm~1624 nm and 1662 nm~1672 nm bands. The results indicate that as aerosol optical depth (AOD) increases, radiance generally increases, with the most significant change observed over vegetated surfaces, which show a 13.26% variation. Within the CO2 and CH4 absorption bands,the increments of CO2/CH4 under equivalent radiation corresponding to the six surface types are ranked: vegetation, metal material, building material, sedimentary finerock, soil, and sedimentary coarserock. Taking soil surface as an example, the study finds that radiance decreases by approximately 0.41 W/m2/μm/sr for every 1 ppm increase in CO2 concentration and by about 0.86 W/m2/μm/sr for every 1 ppb increase in CH4 concentration. Further analysis shows a near-parabolic relationship between AOD and radiance, with consistent trends for CO2 and CH4. As AOD increases, the concentration of both gases exhibit continuous growth. Vegetated surfaces demonstrate the largest concentration changes, with CO2 and CH4 varying by approximately 40.96 ppm and 137.87 ppb, respectively. Explorations under mixed surface conditions indicate that spectral radiance increases with surface albedo, reaching maximum values of 7.7 W/m2/μm/sr for CO2 and 7.45 W/m2/μm/sr for CH4. These findings underscore the critical roles of aerosols and surface albedo in satellite-based greenhouse gas retrievals, offering valuable theoretical guidance for enhancing the accuracy of remote sensing measurements.

Keywords: Aerosol and surface; Remote sensing detection; Greenhouse gases.

1. Introduction

Since the industrial revolution, intensified human activities—particularly the extensive use of fossil fuels such as coal, oil, and natural gas—have disrupted the natural balance among the atmosphere, oceans, and biosphere, leading to a significant rise in greenhouse gas (GHG) concentrations [[1]]. According to the Greenhouse Gas Bulletin published by the World Meteorological Organization (WMO) in 2023, carbon dioxide (CO_2) and methane (CH_4), the two principal atmospheric greenhouse gases, account for approximately 82% of the greenhouse effect. From 1750 to 2023, the global average of CO_2 concentration increased from 280 ppm to 420 ppm, nearly a 1.5-fold rise compared to pre-industrial levels, while the global average CH_4 concentration surged to 2.6 times its pre-industrial level. As of 2023, the global average near-surface temperature has risen by approximately 1.45°C above pre-industrial levels, with China's average temperature increasing by 0.81°C since 1991 [[2]]. Over the past 70 years, China's temperature has shown a particularly pronounced upward trend, warming at an average rate of 0.3°C per decade—nearly double the global average—largely attributed to rapid industrialization. The escalating concentrations of greenhouse gases have not only accelerated global warming but have also amplified the frequency and intensity of extreme weather events, exerting profound impacts on human societies' survival and lifestyles. These challenges underscore the urgency of addressing greenhouse gas emissions and mitigating the far-reaching consequences of climate change [[3],[4]].

There are three main methods of GHG detection: ground-based, airborne and satellite detection. Ground-based detection is the earliest and has established observation system such as the Total Carbon Column Observation Network (TCCON) [[5]] and the Network for Detection of Atmospheric Composition Changes (NDACC) [[6]]. On the airborne front, a series of detectors have also been developed, including the Airborne Laser Infrared Absorption Spectrometer (ALIAS) [[7]] and the second-generation ALIAS (ALIAS-II) [[8]], the Airborne Visible/Infrared Imaging Spectrometer (AVIRIS-Classic) [[9]] and the next-generation AVIRIS (AVIRIS-NG) [[10]], and the Unmanned Aerial Systems Chromatography for Atmospheric Trace Matter Sounding (UCATS) [[11]], etc. While ground-based and airborne observations are highly accurate, they have limited spatial coverage and can only be applied to localized observations. In contrast, satellite observation is not constrained by geographic or natural conditions, enabling sustained and high-precision global monitoring. Satellite

measurements offer valuable "top-down" validation for "bottom-up" emission inventories, supporting large-scale, accurate greenhouse gas monitoring [[12],[13],[14]]. Currently, major satellites dedicated to greenhouse gas monitoring include Sentinel-5p satellite [[15]], which enables global monitoring of CO_2 and CH_4 concentrations via the TROPOMI payload, and satellites in the GOSAT and OCO series, along with point-source monitoring satellites like GHGsat, Methasat and CarbonMapper. Since China launched its first carbon monitoring satellite, TanSat [[16]], in 2016, it has also launched a series of satellites such as GF-5 [[17]], FY-3D [[18]] and DQ-1 [[19]], many of which involve Polarization Cross Fire (PCF) observation modes.

A key challenge in satellite-based GHG monitoring is the selection of appropriate detection bands. Early remote sensing detection of CO_2 concentration mainly relies on the thermal infrared band, which is sensitive to CO_2 concentration in the middle and upper layers but has a large uncertainty in the detection of gas concentration in the bottom layer [[20]], and the information on greenhouse gas concentration can be performed from the data of some comprehensive remote sensing payloads configured with this band, which can satisfy the demand for early greenhouse gas detection. At present, the new generation of on-orbit GHG detection satellite-based passive remote sensing payloads have chosen near-infrared (NIR) bands to realize the detection of GHG concentrations in the lower atmosphere (troposphere and boundary layer) [[21]], and the selected NIR bands are [[22],[23]]: the 1.56 μm CO_2 absorption band and the 1.64 μm CH_4 absorption bands, which are sensitive to CO_2 and CH_4 concentration variations and have few interfering gases, respectively, and are used for inversion of CO_2 and CH_4. In the shortwave infrared region, there are many generalized and combined bands for CO_2 and CH_4 molecules, especially near 1.6 μm. Using this band, CO_2 and CH_4 absorption features can be effectively characterized to obtain CO_2 and CH_4 concentration information. Moreover, short-wave infrared is more sensitive to the near-surface CO_2 and CH_4 concentration changes, which can make up for the shortcomings of thermal infrared [[4],[24]].

The primary requirement for accurate greenhouse gas detection using the solar short-wave infrared band is simulating the solar spectrum through an atmospheric radiative transfer model. The model simulates the value of radiation received by satellite sensors after the solar spectrum has been absorbed, scattered and reflected by the Earth's surface. Satellites measure the energy backscattered by the atmosphere and reflected from the ground, but the scattering of light by aerosols introduces changes in photon behavior within the aerosol layer, altering the optical path length. As a result, aerosol optical properties and surface characteristics are among the most important sources of error in satellite measurements [[25]]. Aerosol scattering can extend the optical path length, potentially causing overestimation of gas concentrations if multiple scattering effects are not properly accounted for in inversion algorithms. Conversely, neglecting the shortening of the optical path length due to backward scattering may lead to underestimation of the actual concentrations [[26]]. The reflectance spectra observed by satellites are highly dependent on surface albedo. Significant variations in the albedo of different surface types result in pronounced differences in the absorption spectra detected by satellites. Surface albedo is therefore a critical factor influencing the accuracy of atmospheric CO_2 and CH_4 concentration measurements. Consequently, understanding the impact of different aerosol properties and surface characteristics on the satellite-observed CO_2 and CH_4 absorption spectra is essential for accurately retrieving CO_2 and CH_4 concentrations.

In summary, this study investigates the influence of varying aerosol optical thicknesses and surface types on satellite-observed radiation, utilizing the LINTRAN radiative transfer model in accordance with the technical specifications of greenhouse gas hyperspectral detection instruments. This approach offers a robust theoretical foundation for analyzing remote sensing error sources in atmospheric CO_2 and CH_4 retrievals via short-wave infrared spectroscopy. Furthermore, it provides valuable technical support for the development of high-precision algorithms for retrieving CO_2 and CH_4 column concentrations.

2. Methods and Principles

2.1. Atmospheric Radiative Transfer Model

The forward modeling of remote sensing by atmospheric satellites characterizes the radiative transfer process, which translates atmospheric and surface variables—primarily including micro-parameters such as aerosols, atmospheric molecules, and greenhouse gases—into the radiance observed at the top of the atmosphere by the satellite. This process can be mathematically expressed as:

$$y = F(x,b) + e_y \tag{1}$$

where y is the measurement vector, x is the state vector, b containing ancillary parameters, e_y represents the measurement error vector, and F denotes the forward model. The measurement vector consists mainly of multi-band intensity and polarization observation information [[27]], which has the Stokes parameters I, Q, U and V [[28]]. as its components:

$$I = [I, Q, U, V]^T \tag{2}$$

the Stokes parameters are calculated by the SRON radiative transfer model LINTRAN v2.0 [[29]]. Using linear polarization degree (*DoLP*) to describe polarization observation, the calculation is as follows:

$$DOLP = \frac{\sqrt{Q^2 + U^2}}{I} \tag{3}$$

In this study, the forward model integrates atmospheric components (greenhouse gases and aerosols), surface characteristics, and vector radiative transfer to simulate the coupling effects between these factors. The aerosol model is categorized into three distinct modes, with the particle size distribution of each mode characterized by a log-normal distribution. Mode one represents fine particles, while modes two and three correspond to insoluble coarse particles and soluble coarse particles, respectively. Mode one primarily consists of inorganic aerosols, black carbon aerosols, and organic carbon aerosols. Mode two is dominated by non-spherical components such as sand and dust, and mode three is mainly composed of inorganic aerosols. The aerosol parameters considered in the model include aerosol optical depth (AOD), effective radius (r_{eff}), effective variance (v_{eff}), sphere fraction (f_{sph}), aerosol layer height (z_{aer}) and the refractive index coefficients corresponding to the standard spectra of each modal component [[30]].

To describe the surface, the surface reflection matrix $R_{surf}(\lambda, \theta s, \theta v, \varphi)$ is given by

$$R_{\text{surf}}(\lambda,\theta_s,\theta_v,\varphi) = r_{11}(\lambda,\theta_s,\theta_v,\varphi)D + R_{pol}(\theta_s,\theta_v,\varphi) \quad (4)$$

where λ is the wavelength; θ_s and θ_v are the sun zenith angle and view zenith angle, respectively; φ is the relative azimuth angle; D is a null matrix except D_{11} = 1, r_{11} $(\lambda,\theta_s,\theta_v,\varphi)$ is described by the Ross–Li bi-directional reflection distribution function (BRDF) model [[30]],

$$r_{11}(\lambda,\theta_s,\theta_v,\varphi) = A(\lambda)(1 + k_{geo}\, f_{geo}(\theta_s,\theta_v,\varphi) + k_{vol}\, f_{vol}(\theta_s,\theta_v,\varphi)) \quad (5)$$

where $A(\lambda)$ is the isotropic reflectance; f_{geo} $(\theta_s,\theta_v,\varphi)$ and f_{vol} $(\theta_s,\theta_v,\varphi)$ are the geometric (Li-Sparse) kernel and volumetric (Ross-Thick) kernel function, respectively; and k_{geo} and k_{vol} are the coefficients for the Li-Sparse and Ross-Thick respectively [[31]].

Table 1. Aerosol parameters in the forward models. c1, c2 and c3 correspond to coefficients for standard refractive index of inorganic aerosol (INORG), black carbon (BC), organic carbon (OC) and dust (DU) [[30]].

Property		Full name	Parameter Setting
Fine mode	r_{eff}	Effective radius (mode 1)	0.15
	v_{eff}	Effective variance (mode 1)	0.2
	AOD	Aerosol optical depth (mode 1)	0.05-1.0
	f_{sph}	Spherical fraction (mode 1)	1.0
	z_{aer}	Aerosol layer height (mode 1)	2000
	c_1(INORG)	Refractive index coefficient (INORG)	0.95
	c_2(BC)	Refractive index coefficient (BC)	0.01
	c_3(OC)	Refractive index coefficient (OC)	0.02
Coarse insoluble mode	r_{eff}	Effective radius (mode 2)	1.0
	v_{eff}	Effective variance (mode 2)	0.6
	AOD	Aerosol optical depth (mode 2)	0.05-1.0
	f_{sph}	Spherical fraction (mode 2)	0.0
	z_{aer}	Aerosol layer height (mode 2)	2000
	c_1(DUST)	Refractive index coefficient (DUST)	1.0
Coarse soluble mode	r_{eff}	Effective radius (mode 3)	2.5
	v_{eff}	Effective variance (mode 3)	0.6
	AOD	Aerosol optical depth (mode 3)	0.05-1.0
	f_{sph}	Spherical fraction (mode 3)	1.0
	z_{aer}	Aerosol layer height (mode 3)	500
	c_1(INORG)	Refractive index coefficient (INORG)	0.9

For the surface types, six surface types were considered: soil, vegetation, sedimentary finerock, sedimentary coarserock, building material, metal material. Except for vegetation, the reflectance spectra of other surface types lack distinct peaks and valleys. The reflectance of soil is influenced by factors such as particle size, water content, and organic matter content. Rock reflectance spectra are primarily affected by mineral composition, degree of weathering, and other geological factors. Both soil and sedimentary coarserock exhibit water absorption features at 1.4 μm and 1.9 μm. Man-made surfaces were categorized into two types: building material and metal material. Building material, including concrete and asphalt, typically exhibit low and stable reflectance values around 0.3, with a relatively flat spectral curve. Metallic material, on the other hand, have even lower reflectance, with their spectral characteristics largely determined by surface roughness and the degree of oxidation. The reflectance spectrum of the vegetation follows a unique pattern that can be divided into three distinct regions. In the visible band, vegetation exhibits a small reflectance peak at approximately 0.55 μm, flanked by absorption features at 0.35 μm and 0.67 μm, caused by chlorophyll absorption of blue and red light while reflecting green light. In the near-infrared band, vegetation reflectance shows a characteristic "steep slope" with a peak near 1.1 μm, creating a distinct spectral signature.

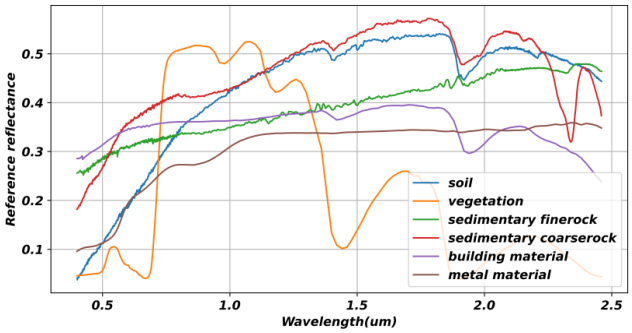

Fig. 1 Reference reflectance for soil, vegetation, sedimentary finerock, sedimentary coarserock, building material and metal material. The data were downloaded from ASTER spectral library.

In the standard setup, the model atmosphere is discretized into 20 homogeneous vertical layers. The vertical profile data for CO_2 and CH_4 were obtained from the American Standard Atmospheric Profile Information [[32]]. Basic atmospheric

parameters, including temperature, humidity and pressure, were read from the NCEP reanalysis data. The absorption coefficients and diffusion characteristics of greenhouse gases at various wavelengths and spectral resolutions were calculated using the Absorption Cross Section and HighResolution Transmittance Database HITRAN [[33]]. The solar zenith angle (SZA) was set to 60°. In this study, the forward model mainly consists of an atmospheric model (greenhouse gases, aerosols) and a surface model, as well as a vector radiative transfer that couples them. The overall framework of the forward model is outlined below:

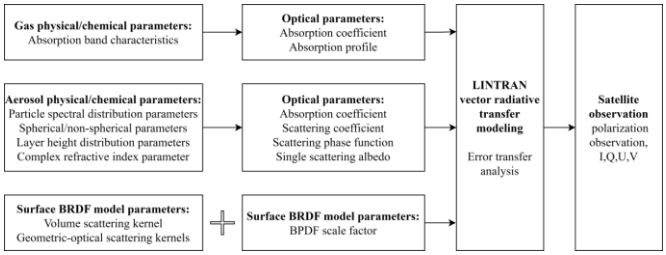

Fig.2 Forward Modeling Flowchart.

2.2. Assessment methodology

This study primarily examined the influence of varying AOD and surface albedo on the radiance of CO_2 and CH_4. The rate of change in radiance under these conditions is expressed by the following equation [[34]]:

$$R\_change_n = \frac{R_n - R_0}{R_0} \times 100\% \tag{6}$$

According to the 20th Global Greenhouse Gases Bulletin published by the World Meteorological Organization [[35],[36]], the average annual increase in concentration of CO_2 is 2.3 ppm, while the average annual increase in concentration of CH_4 is 11 ppb. In this study, the average concentration of CO_2 and CH_4 provided in the bulletin was used as the initial value, and the annual increase was taken as the magnitude of the change in concentration. The initial CO_2 concentration was set to 420 ppm, with simulations conducted under clear-sky conditions. The CO_2 concentration was subsequently adjusted to 422.3 ppm, reflecting an increase of 2.3 ppm. Similarly, the initial CH_4 concentration was set to 1934 ppb, with an adjustment of 11 ppb. The average radiance change corresponding to a 1 ppm increase in CO_2 (or a 1 ppb increase in CH_4) was calculated using the following formula, where $\bar{R}$ indicates the average value of radiance. For CO_2, *wave* refers to the spectral ranges 1601 nm~1604 nm and 1607 nm~1611 nm, while for CH_4, *wave* corresponds to 1665 nm~1667 nm.

$$\begin{aligned} \bar{R}(\Delta 1 ppm) &= \frac{\left[\bar{R}_{wave}(422.3 ppm) - \bar{R}_{wave}(420 ppm)\right]}{2.3 ppm} \\ \bar{R}(\Delta 1 ppb) &= \frac{\left[\bar{R}_{wave}(1945 ppb) - \bar{R}_{wave}(1934 ppb)\right]}{11 ppb} \end{aligned} \tag{7}$$

The CO_2 concentration is determined by dividing the average radiance value within the high-sensitivity band by the radiance value corresponding to a 1 ppm change under identical conditions. The calculation method for CH_4 follows the same approach as that for CO_2.

$$\begin{aligned} \Delta CO_{2(n)} &= \frac{\left(\bar{R}_{wave(n)} - \bar{R}_{wave(n-1)}\right)}{\bar{R}(\Delta 1 ppm)} \\ \Delta CH_{4(n)} &= \frac{\left(\bar{R}_{wave(n)} - \bar{R}_{wave(n-1)}\right)}{\bar{R}(\Delta 1 ppb)} \end{aligned} \tag{8}$$

3. Sensitivity Experiment

3.1. Initial Sensitivity Analysis of CO2 and CH4 Concentration

In this study, an atmospheric radiative transfer model was employed to examine the impact of a 1 ppm or 1 ppb change in CO_2 and CH_4 concentrations on the spectral radiation. The spectral resolution used in the simulation was 0.12 nm, with the wavelength range was 1594 nm ~1624 nm for CO_2 and 1662 nm ~1672 nm for CH_4. For demonstration purposes, soil was selected as the surface type, and the AOD was set to 0.1. When the initial CO_2 concentration was adjusted by 2.3 ppm, the rate of change in radiance ranged from -0.16% to 0%. The bands near 1594 nm~1596 nm showed the smallest rate of change in radiance due to the change in CO_2 concentration, indicating that these bands are not sensitive to the change in CO_2 concentration. On the other hand, the maximum sensitivity of -0.16% for the bands near 1601 nm~1604 nm indicates that these bands are very sensitive to changes in CO_2 concentration and that these absorption peaks are relatively densely located. Since the depth of the absorption peaks varies between wavelengths, in order to facilitate the adjustment of the calculation of the initial CO_2 value, the interval of -0.1% to -0.16% change in radiance brightness was selected as the highly sensitive bands for CO_2, and about 58 specific bands in the ranges of 1601 nm~1604 nm and 1607 nm~1611 nm were finally identified, and their average values were calculated, and it was found that for every 1 ppm increase in the concentration of CO_2 , the radiance decreases by about 0.406063 W/m^2/um/sr over these 58 specific bands($\bar{R}(\Delta 1 ppm)$).

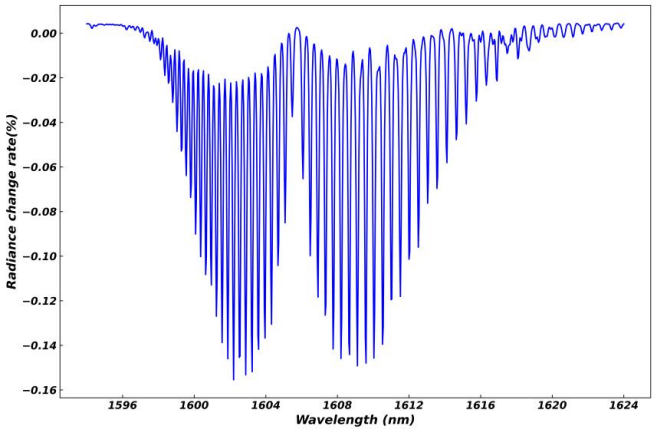

Fig.3 Radiance change rate for CO2 with an initial estimate of 420 ppm and a variation of 2.3 ppm for AOD@550nm is 0.1 and for soil surface.

When the initial value of CH_4 is adjusted by 11 ppb, the range of radiance change rate is from -0.21% to 0%. The depth of the absorption peaks of CH_4 is not as intensive as that of CO_2, which is mainly manifested near the 1666 nm band. In order to facilitate the adjustment of the calculation of the initial CH_4 value, the radiance change rate of -0.1% to -0.22% interval was selected as the highly sensitive bands of CH_4, and

about 21 specific bands in the range of 1665 nm~1667 nm were finally identified and their average values were calculated, and it was found that for every increase of 1 ppb in the concentration of CH_4, the radiance decreases by about 0.861274 W/m^2/um/sr($\bar{R}(\Delta 1 ppb)$).

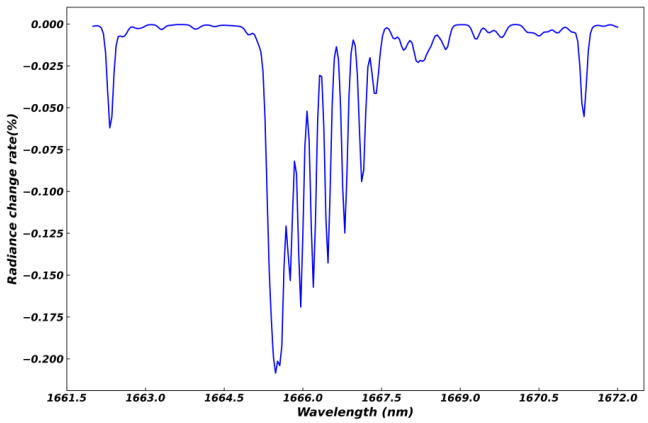

Fig. 4 Radiance change rate for CH4 with an initial estimate of 1934 ppb and a variation of 11 ppb for AOD@550nm is 0.1 and for soil surface.

3.2. Influence of aerosol and surface albedo on CO2, CH4 radiance

The figure below illustrates the variations in CO_2 radiance across different surface types under varying AOD. As the AOD increases from 0.05 to 1.0, a consistent upward trend in radiance is observed. This rise in AOD corresponds to a higher concentration of aerosol particles in the atmosphere, which significantly enhances their scattering and absorption of light, thereby increasing atmospheric radiance. Notable fluctuations are evident under varying AOD conditions. Among the surface types, sedimentary coarserock and soil exhibits the most pronounced radiance changes, transitioning across three distinct color ranges (gray-purple-green) as AOD varies. In contrast, vegetation predominantly appears in blue, indicating minimal radiance variation. The radiance changes of sedimentary finerock and building material are nearly identical due to their similar reflectance properties, with green and orange dominating their color spectrum. In the CO_2 strong absorption bands (1601 nm~1604 nm and 1607 nm~1611 nm), sedimentary coarserock surfaces exhibit the highest radiance values, followed by soil, sedimentary finerock, building material, metal material, and vegetation in descending order. This ranking aligns with the surface reflectance characteristics of these materials in the 1.6 μm band.

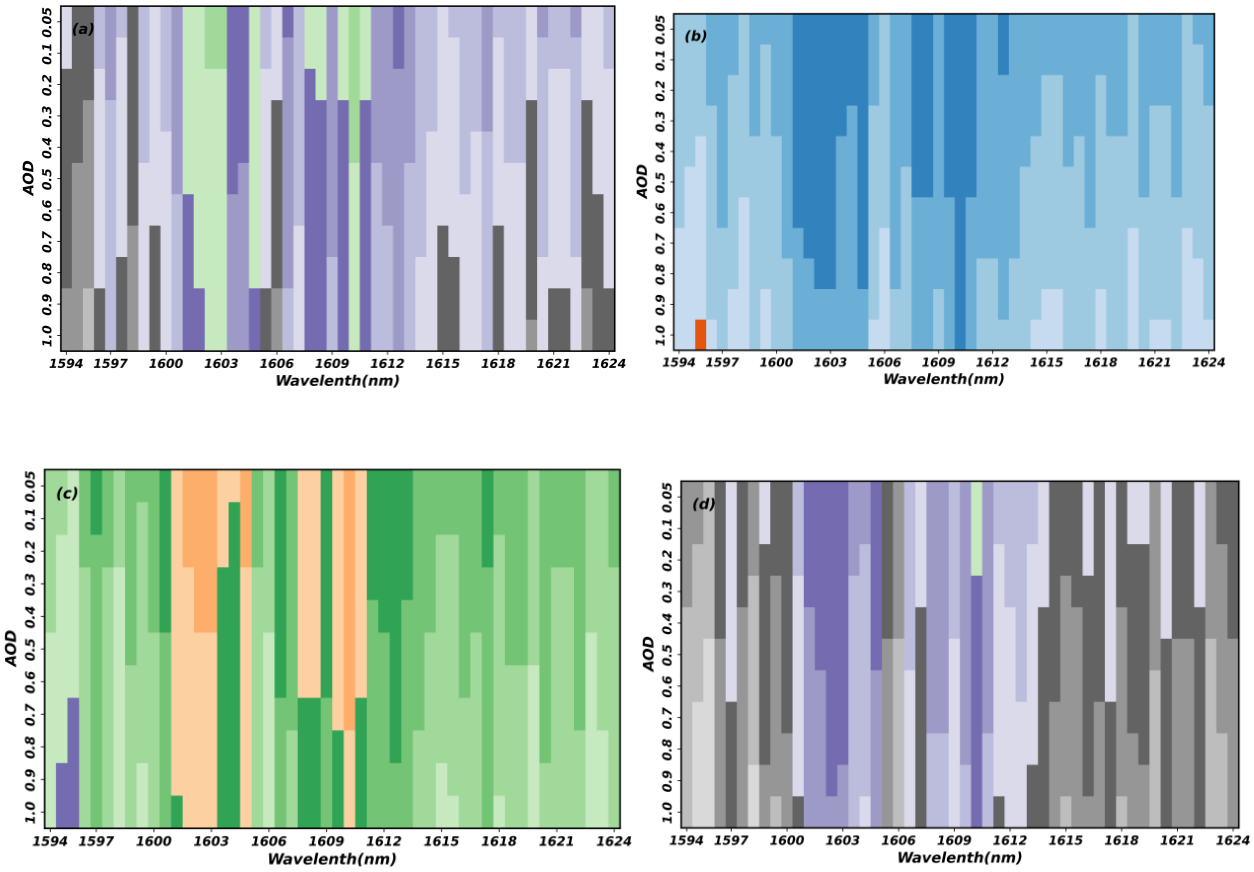

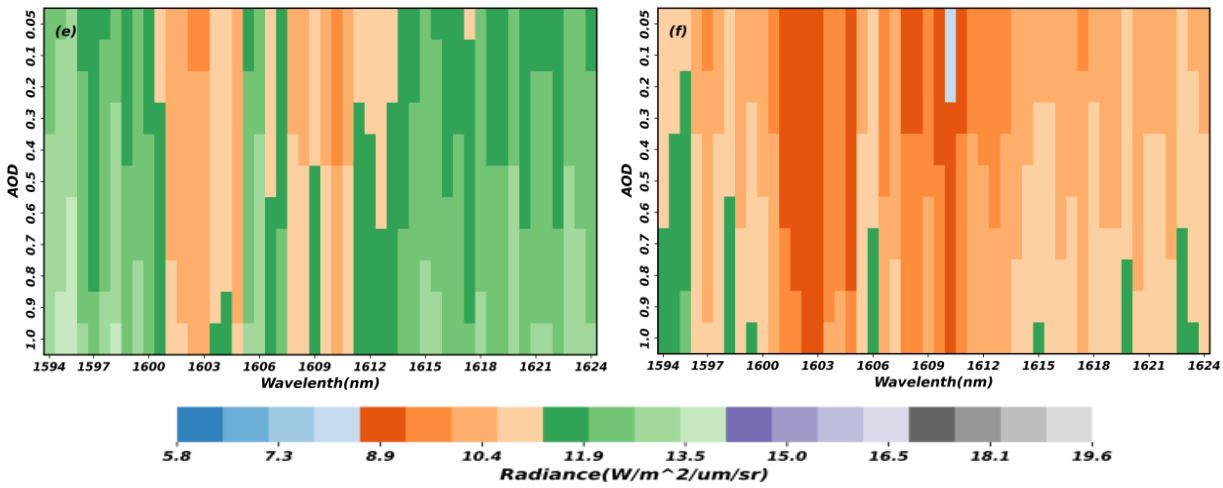

Fig. 5 CO2 Radiance at different AOD for different surface types. (a)soil; (b)vegetation; (c)sedimentary finerock; (d)sedimentary coarserock; (e)building material; (f)metal material

Similar to CO_2, the radiance of CH_4 also increases progressively with the rise in AOD. As shown in the figure, CH_4 radiance is notably higher in the weak absorption bands (1662.5 nm~1665 nm and 1667 nm~1672 nm) and lower in the strong absorption band (1665 nm~1667 nm). Among surface types, soil and sedimentary coarserock exhibit the most pronounced variations in radiance, appearing predominantly gray and purple in the weak absorption bands and green in the strong absorption band. In contrast, vegetation shows the least variation, with orange dominating the weak absorption bands and blue prevailing in the strong absorption band. Within the CH_4 strong absorption band,sedimentary coarserock surface display the highest radiance values, followed in descending order by soil,sedimentary finerock, building material, metal material, and vegetation.In summary, the combined effects of surface albedo and AOD govern the variations in atmospheric radiance. Under high-albedo conditions, increased surface reflectance significantly amplifies aerosol scattering, resulting in a notable rise in atmospheric radiance, as observed over soil and sedimentary coarserock. These findings reveal the synergistic mechanisms between aerosols and surface albedo in shaping atmospheric radiative characteristics.

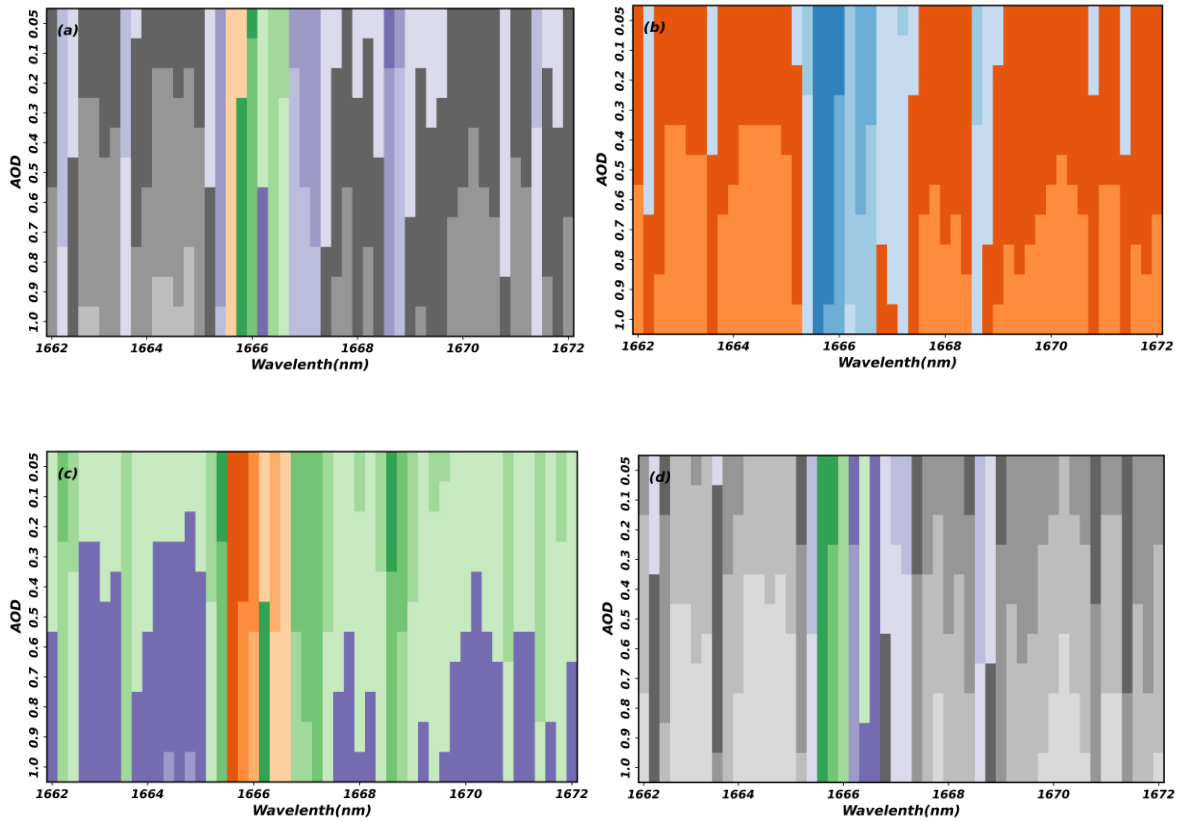

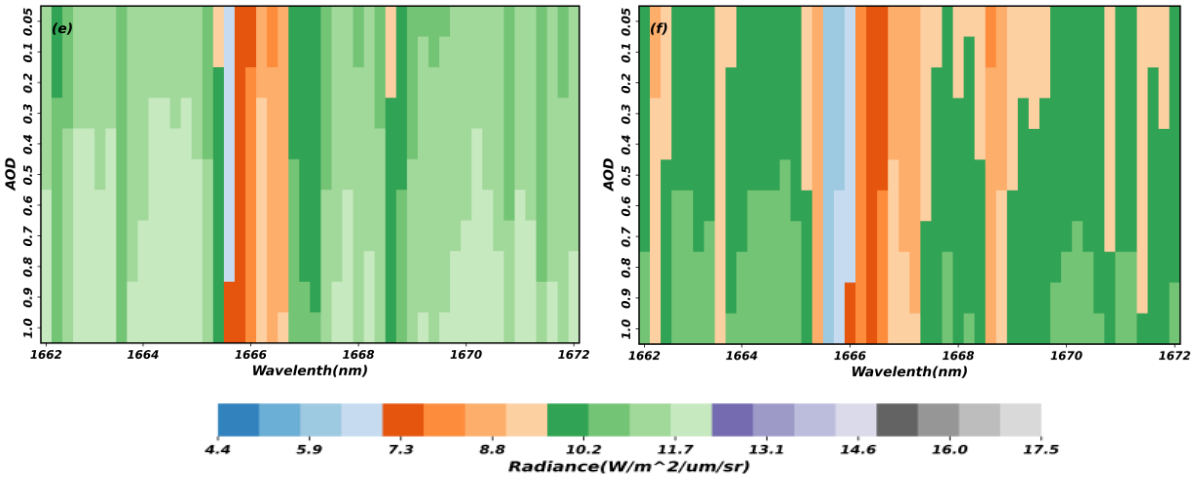

Fig. 6 CH4 Radiance at different AOD for different surface types. (a)soil; (b)vegetation; (c)sedimentary finerock; (d)sedimentary coarserock; (e)building material; (f)metal material

The rate of change of CO_2 and CH_4 radiance at varying AOD levels was calculated using the AOD-neutral case as a standard reference, with radiance differences derived from the highly sensitive bands identified in Section 3.1. The results are shown below. By comparing the spectral changes induced by each 1 ppm or 1 ppb increase in CO_2 and CH_4 concentrations, a relationship between AOD and changes in CO_2 and CH_4 concentrations was established. The study reveals a consistent trend between CO_2 and CH_4 concentrations.With the increase of AOD, the concentrations of both gases show a continuous growth trend. However, when AOD reaches a high value, the rate of concentration growth begins to slow down. This finding aligns with findings from the SRON team in the Netherlands on CO_2 inversion for the CO2M satellite, which noted that for fine aerosols in the boundary layer, the XCO_2 bias is estimated to be limited but still slightly grows for larger AOD. Additionally, for coarse aerosols around 8 km altitude, such as dust and thin cirrus, the XCO_2 bias is also dependent on AOD but is estimated to be several ppm [[37]]. These results corroborate our forward modeling process, where the gas concentration growth rate similarly diminishes at higher AOD values. This nuanced relationship underscores the complex interplay between AOD and gas concentration, highlighting the existence of a critical AOD level that balances the competing effects of aerosols on gas detection.Among the various surface types, the variations of approximately 40.96 ppm and 137.87 ppb, respectively. The magnitude of changes in gas concentrations across surface types ranked in descending order is as follows: vegetation, metal material, building material, sedimentary finerock, soil, and sedimentary coarserock. Due to the similar surface albedo of soil and coarserock, their AOD-induced changes in CO_2 and CH_4 concentrations exhibited nearly identical trends, resulting in overlapping curves.

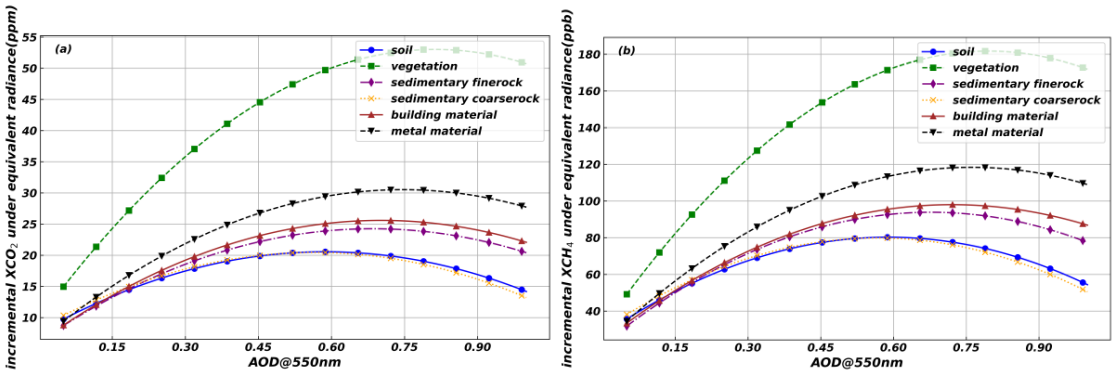

Fig. 7 Incremental XCO2/XCH4 under equivalent radiance for AOD@550nm. (a)XCO2; (b)XCH4(XCO2 and XCH4 are calculated from Eq. (8).)

Table 2. The equation coefficients between AOD@550nm and gas concentration changes.

surface type	AOD@550nm & CO_2			AOD@550nm & CH_4		
	a	*b*	*c*	*a*	*b*	*c*
soil	-37.44	43.98	7.64	-153.36	180.72	27.02
vegetation	-65.42	106.35	9.79	-238.36	379.39	30.76
sedimentary finerock	-38.58	52.81	6.18	-157.67	213.59	21.52
sedimentary coarserock	-38.18	43.10	8.29	-156.25	177.06	29.68
building material	-39.53	55.50	6.11	-143.54	206.93	23.41
matal material	-43.59	65.02	6.27	-165.61	252.21	22.34

The variation of AOD demonstrates an almost parabolic relationship with the concentration changes of CO_2 and CH_4, with the fitting curve following a quadratic form. The equations are expressed as $y=ax^2+bx+c$,where y represents

the gas concentration, *a*, *b* and *c* are coefficients derived from the fitting process, and *x* denotes the AOD. The curve equation coefficients for the six surface types are shown in the table below. With the exception of vegetation, the gas concentration values for all other surface types remain nearly constant and show minimal variation when the AOD is 0.05.

3.3. Simulation and analysis of CO2 and CH4 based on mixed surface

In this study, the variations in CO_2 and CH_4 radiance across six different surface types were analyzed, with a particular focus on the impact of mixed surfaces on the remote sensing detection of greenhouse gases in the short-wave infrared 1.6 μm [[38]]. The mixed surface simulation involved a random mixture of soil and vegetation, with aerosol parameters and SZA settings consistent with those used in previous studies (see Section 2). Additionally, the CH_4 concentration was fixed at 1934 ppb, and the CO_2 concentration was set at 420 ppm. As shown in the figure, the figure demonstrates the influence of CO_2 and CH_4 radiance brightness in the absorbing band by the magnitude of AOD. The CO_2 and CH_4 radiance gradually increases with increasing AOD. In the strong absorption bands of CO_2 and CH_4, the radiance varies more gently and does not show significant fluctuations.

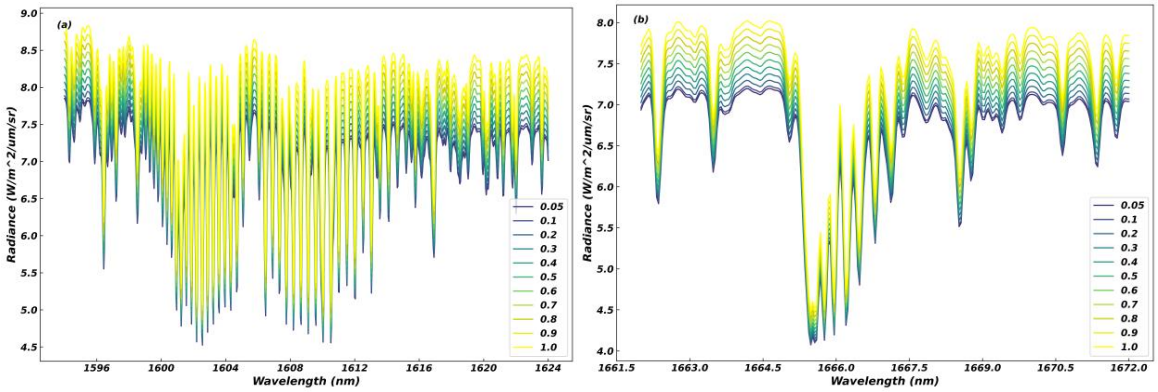

Fig. 8 Radiance for AOD@550nm range from 0.05 to 1.0 and mixed surface. (a)CO2; (b)CH4

By grouping and calculating the radiance under mixed surface conditions, the average radiance values is calculated for various combinations of AOD and Albedo. As illustrated in the figure, these combinations have a pronounced effect on the radiance of CO_2 and CH_4. The analysis reveals that both CO_2 and CH_4 radiances generally increase with higher AOD and albedo, reaching maximum average values of 7.7 $W/m^2/\mu m/sr$ and 7.45 $W/m^2/\mu m/sr$, respectively. At low AOD values, variations in surface albedo exert minimal influence on radiance, as indicated by the deep blue regions in the figure. However, CO_2 radiance is more sensitive to changes in AOD compared to CH_4, with radiance transitioning to a yellow hue as AOD increases to 1.0. This highlights the stronger dependence of CO_2 radiance on atmospheric aerosol content.

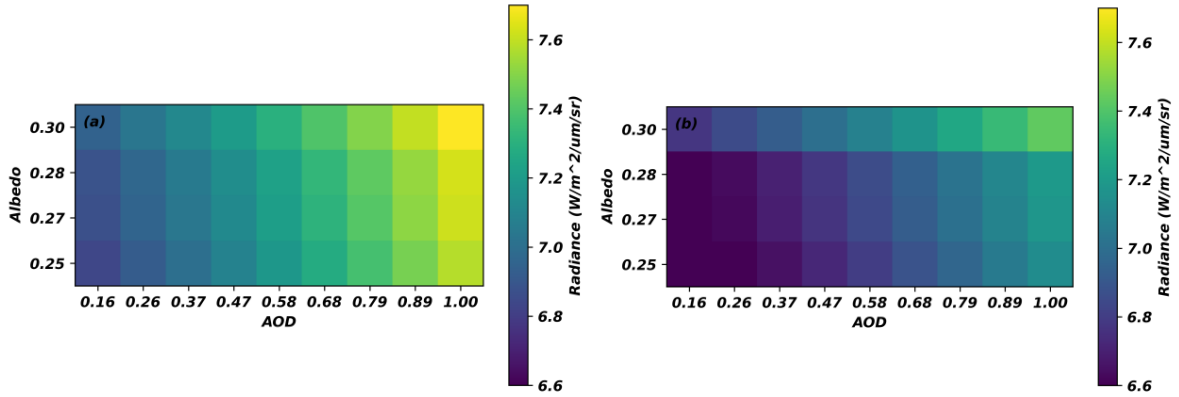

Fig. 9 The average radiance over 1594nm~1624nm and 1662nm~1672nm for different AOD@550nm and albedo for mixed surface. (a)CO2 is 420ppm; (b)CH4 is 1934ppb

4. Conclusion

This article quantitatively analyzes the effects of AOD and surface albedo on atmospheric CO_2 and CH_4 detection using the LINTRAN radiative transfer model. First, the concentration changes of CO_2 and CH_4 were calculated to determine the corresponding radiance values. A sensitivity analysis of six surface types and AOD parameters was established to evaluate their impact on the concentration values of CO_2 and CH_4. Subsequently, the relationship between radiance, AOD, and albedo was explored under mixed surface conditions. The main research conclusions are as follows:

As the aerosol optical depth (AOD) increases, the radiance generally shows an upward trend. The radiance change is most pronounced for the vegetation surface, with a change rate of 13.26%. In the absorption bands of CO_2 and CH_4, the six surface types are ranked in descending order of radiance variation as follows: vegetation, metal material, building material, sedimentary finerock, soil and sedimentary coarserock. Represented by bare soil surface, research has found that for every 1ppm increase in CO_2 concentration, the radiance decreases by approximately $0.41 W/m^2/um/sr$; For every 1 ppb increase in CH_4 concentration, the radiance decreases by approximately 0.86 $W/m^2/um/sr$. Further analysis showed that the changes of AOD and gas concentration were nearly parabolic, and the trends of CO_2 and CH_4 were consistent. With the increase of AOD, the

concentration of both gases showed a continuous increase. Under vegetation surface types, the changes in CO_2 and CH_4 concentrations are most significant, with variations of approximately 40.96 ppm and 137.87 ppb, respectively. Further exploration based on mixed surface conditions shows that as the surface albedo increases, the observed spectral radiance also increases, with the maximum radiance values of CO_2 and CH_4 reaching 7.7 W/m^2/um/sr and 7.45 W/m^2/um/sr, respectively.

Funding

This work is supported by the National Key R&D Program of China (Grant No:2023YFB3907405) and the National Natural Science Foundation of China (Grant No. 42305151).

Acknowledgment

Min Li thanks the Aerospace Information Research Institute of Chinese Academy of Sciences for its joint training. We thank the SRON team in the Netherlands for providing the LINTRAN radiative transfer model.

Disclosures

The authors declare that there are no conflicts of interest related to this paper.

Data availability

We appreciate the information provided by AFGL US standard profile and NCEP reanalysis data. We thank the USGS team for providing the ASTER geophysical spectral database.

References

[1] L. Bruhwiler, S. Basu, J. H. Butler, et al., "Observations of greenhouse gases as climate indicators," Climatic Change, 165(1), 12 (2021).

[2] Climate Change Center, China Meteorological Administration, "Blue Paper of Climate Change 2019 in China," China Meteorological Administration, Beijing, (2019).

[3] Y. K. Gautam, K. Sharma, S. Tyagi, et al., "Nanostructured metal oxide semiconductor-based sensors for greenhouse gas detection: progress and challenges," Royal Society Open Science, 8(3), 201324 (2021).

[4] Q. S. Wang, H. Y. Luo, Z. W. Li, et al., "Research progress of spaceborne passive remote sensing detection payload of greenhouse gases," National Remote Sensing Bulletin, 27(4), 857-870 (2023).

[5] D. Wunch, G. C. Toon, J. F. L. Blavier, et al., "The total carbon column observing network," Philosophical Transactions of the Royal Society A, 369(1943), 2087-2112 (2011).

[6] M. De Mazière, A. M. Thompson, M. J. Kurylo, et al., "The Network for the Detection of Atmospheric Composition Change (NDACC): history, status and perspectives," Atmospheric Chemistry and Physics, 18(7), 4935-4964 (2018).

[7] C. R. Webster, R. D. May, C. A. Trimble, et al., "Aircraft (ER-2) laser infrared absorption spectrometer (ALIAS) for in situ stratospheric measurements of HCl, N2O, CH4, NO2, and HNO3," Applied Optics, 33(3), 454-472 (1994).

[8] D. C. Scott, R. L. Herman, C. R. Webster, et al., "Airborne Laser Infrared Absorption Spectrometer (ALIAS-II) for in situ atmospheric measurements of N2O, CH4, CO, HCl, and NO2 from balloon or remotely piloted aircraft platforms," Applied Optics, 38(21), 4609-4622 (1999).

[9] G. Vane, M. Chrisp, H. T. Enmark, et al., "Airborne Visible/Infrared Imaging Spectrometer (AVIRIS): an advanced tool for Earth remote sensing," Remote Sensing: From Res. Towards Operational Use, 2, 751-757 (1984).

[10] A. K. Thorpe, C. Frankenberg, A. D. Aubrey, et al., "Mapping methane concentrations from a controlled release experiment using the next generation airborne visible/infrared imaging spectrometer (AVIRIS-NG)," Remote Sensing of Environment, 179, 104-115 (2016).

[11] E. J. Hintsa, F. L. Moore, D. F. Hurst, et al., "UAS Chromatograph for Atmospheric Trace Species (UCATS): a versatile instrument for trace gas measurements on airborne platforms," Atmospheric Measurement Techniques, 14(10), 6795-6819 (2021).

[12] Y. Liu, J. Wang, K. Che, et al., "Satellite remote sensing of greenhouse gases: progress and trends," National Remote Sensing Bulletin, 25(1), 53-64 (2021).

[13] Z. Q. Li, Y. S. Xie, Y. S. Shi, et al., "A review of collaborative remote sensing observation of greenhouse gases and aerosol with atmospheric environment satellites," National Remote Sensing Bulletin, 26(5), 795-816 (2022).

[14] Z. He, Z. Q. Li, C. Fan, et al., "Satellite Sensors and Retrieval Algorithms of Atmospheric Methane," Acta Optica Sinica, 43(18), 1899904 (2023).

[15] A. Lorente, T. Borsdorff, A. Butz, et al., "Methane retrieved from TROPOMI: improvement of the data product and validation of the first 2 years of measurements," Atmospheric Measurement Techniques, 14(1), 665-684 (2021).

[16] Y. Liu, J. Wang, L. Yao, et al., "The TanSat mission: preliminary global observations," Science Bulletin, 63(18), 1200-1207 (2018).

[17] W. Xiong, "Greenhouse gases Monitoring Instrument (GMI) on GF-5 satellite (invited)," Infrared and Laser Engineering, 48(3), 0303002 (2019).

[18] Q. F. Lu, F. Zhou, C. L. Qi, et al., "Spectral performance evaluation of high-spectral resolution infrared atmospheric sounder onboard FY-3D," Optics and Precision Engineering, 27(10), 2105-2115 (2019).

[19] G. Han, H. Xu, W. Gong, et al., "Feasibility study on measuring atmospheric CO2 in urban areas using Spaceborne CO2-IPDA LIDAR," Remote Sensing, 10(7), 985 (2018).

[20] F. M. Bréon, P. Ciais, "Spaceborne remote sensing of greenhouse gas concentrations," Comptes Rendus Geoscience, 342(4/5), 412-424 (2010).

[21] Y. Yoshida, Y. Ota, N. Eguchi, et al., "Retrieval algorithm for CO2 and CH4 column abundances from short-wavelength infrared spectral observations by the Greenhouse gases observing satellite," Atmospheric Measurement Techniques, 4(4), 717-734 (2011).

[22] A. Butz, S. Guerlet, O. Hasekamp, et al., "Toward accurate CO2 and CH4 observations from GOSAT," Geophysical Research Letters, 38(14), L14812 (2011).

[23] A. Bril, S. Maksyutov, D. Belikov, et al., "EOF-based regression algorithm for the fast retrieval of atmospheric CO2 total column amount from the GOSAT observations," Journal of Quantitative Spectroscopy and Radiative Transfer, 189, 258-266 (2017).

[24] M. Li, C. Fan, Z. Li, et al., "Simulation study on aerosol and greenhouse gas synergy based on polarization and hyperspectral combination," Acta Optica Sinica, 45(06), 13 (2025).

[25] J. Chen, C.M. Zhang, D.Y. Wang, et al., "Effects of the surface albedo on short-wave infrared detection of atmospheric CO2," Acta Phys. Sin., 64(23), 239201 (2015).

[26] Q. Wang, Y.M. Bi, Z.D. Yang, et al., “Simulation analysis of aerosol effect on shortwave infrared remote sensing detection of atmospheric CO2,” Acta Phys. Sin., 67(3), 039202 (2018).

[27] S. Lu, J. Landgraf, G. Fu, et al., “Simultaneous retrieval of trace gases, aerosols, and cirrus using RemoTAP—The global orbit ensemble study for the CO2M mission,” Front. Remote Sens., 3, 914378 (2022).

[28] S. Chandrasekhar, “Radiative Transfer,” Dover Publications, Inc., New York (1960).

[29] D. Schepers, J. M. J. aan de Brugh, P. Hahne, et al., “LINTRAN v2.0: A Linearised Vector Radiative Transfer Model for Efficient Simulation of Satellite-Born Nadir-Viewing Reflection Measurements of Cloudy Atmospheres,” J. Quant. Spectrosc. Radiat. Transfer 149, 347-359 (2014).

[30] Z. Zhang, G. Fu, O. Hasekamp, et al., “Aerosol retrieval over snow using the RemoTAP algorithm,” Atmos. Meas. Tech. 16, 6051-6063 (2023).

[31] W. Wanner, X. Li, A. H. Strahler, et al., “On the derivation of kernels for kernel-driven models of bidirectional reflectance,” J. Geophys. Res.-Atmos. 100, 21077-21089 (1995).

[32] O. P. Hasekamp, A. Butz, “Efficient Calculation of Intensity and Polarization Spectra in Vertically Inhomogeneous Scattering and Absorbing Atmospheres,” J. Geophys. Res. Atmos. 113 (2008).

[33] L. S. Rothman, I. E. Gordon, A. Barbe, et al., “The HITRAN 2008 molecular spectroscopic database,” J. Quant. Spectrosc. Radiat. Transfer 110, 533-572 (2009).

[34] Z. Wu, M. Li, K. Rao, et al., “An improved band design framework for atmospheric pollutant detection and its application to the design of satellites for CO2 observation,” J. Quant. Spectrosc. Radiat. Transf., 309, 108712 (2023).

[35] World Meteorological Organization, “The 20th Global Greenhouse Gas Bulletin,” World Meteorological Organization, Geneva, (2024).

[36] D. Hou, X. Meng, M. Qin, et al., “Nitrous oxide (N2O) emission characteristics of farmland (rice, wheat, and maize) based on different fertilization strategies,” PLOS ONE, 19(7), e0305385 (2024).

[37] Y. Meijer,H. Boesch,A. Bombelli ,et al., “Copernicus CO2 Monitoring Mission Requirements Document,” [EOP-SM/3088/YM-ym], (2020).

[38] Y. Liu, J. Chen, Y. Shi, et al., “Global Emissions Inventory from Open Biomass Burning (GEIOBB): utilizing Fengyun-3D global fire spot monitoring data,” Earth Syst. Sci. Data, 16, 3495-3515 (2024).